Composition of the Earth and implications for geodynamics

William F. McDonough* [1,2,3]

[1]Department of Geology, University of Maryland, College Park, MD 20742, USA
[2]Department of Earth Science, Tohoku University, Sendai, Miyagi 980-8578, Japan
[3]Research Center for Neutrino Science, Tohoku Univ., Sendai, Miyagi 980-8578, Japan

May 18, 2023

submitted to: Chemical geodynamics of the Earth's mantle: new paradigms

Abstract

The composition of the bulk silicate Earth (BSE) is the product of planetary accretion, core differentiation, and Moon formation. By establishing the composition of the BSE one can determine the composition of the bulk Earth and by subtraction calculate the core's composition. The BSE represents the bulk Earth minus the core, which in today's terms equals the modern mantle, the continental crust, and the hydrosphere-atmosphere systems. The modern mantle can be framed in terms of two compositionally distinct components, an enriched and a depleted mantle, with the latter as the MORB (mid-ocean ridge basalt) source and the former as the OIB (ocean island basalt) source.

The Earth's surface heat flux is 46±3 TW (terrawatts, 10^{12} watts). Some fraction of this flux (∼40% or ∼20 TW) is derived from radioactive heat produce by the decay of U, Th, and K. Some 40% of the Earth's budget of these elements is stored in the continental crust (∼7.7 TW) and does not contribute to mantle heating. The remaining energy is primordial derived from accretion and core separation. The heat

*Corresponding author -WFM: ORCID number: 0000-0001-9154-3673; E-mail: mcdonoug@umd.edu

flux through the mantle also includes a core contribution ($\sim$10$\pm$5 TW; i.e., bottom heating of the mantle).

The rich record of seismic tomography documents ocean slabs stagnating at the base of the transition zone, others stagnating at $\sim$1000 km depth, and others plunge directly into the deep mantle. Collectively, these images reveal mass exchange between the upper and lower mantle and are consistent with whole mantle convection. The Mantle Transition Zone (MTZ) plays a major role in the differentiation of mantle. Mantle dynamics is controlled by it's viscosity, which in turn is controlled by its water content and temperature. Evidence for core-mantle exchange remains elusive. Documented Hadean ^{182}W/^{184}W isotopic anomalies coupled with primordial noble gas signatures in OIBs presents a preservation challenge for mantle convection models.

1 Structure of the Earth

1.1 Definition of its domains (core – mantle – crust)

Earth's structure is composed of compositionally distinct, concentric shells: a metallic core surrounded by a silicate shell and this is surrounded by a hydrosphere/atmosphere. Our understanding of the chemical and isotopic compositions of these domains decreases with depth, resulting in significant uncertainties in the composition of the deep mantle and core. All terrestrial planets share this differentiated structure of a core, mantle and crust.

1.2 PREM

Dziewonski and Anderson (1981) presented a 1D seismic model for the Earth. This model, based on body waves and free oscillation data for the Earth, is used to define the depth to the core mantle boundary (CMB), documents the liquid outer and solid inner core, and provides a density gradient for the Earth's interior. Importantly, PREM documents jumps in the velocity of the compressional (V_p) and shear (V_s) waves at different depths in the mantle, which correspond to observed phase changes in the abundant silicate minerals.

Figure 1 and Table 1 provides a reference state for Earth's interior. The temperatures reported are for the major phase changes in the mantle and represent the post-phase change in temperature. Major phase changes in the mantle occur at 410 km, 520 km, and 660 km for a pyrolite composition having an Mg# of 0.89 (where Mg# = atomic proportions of Mg/(Mg+Fe)). At 410 and 520 km depths the isochemical ($(Mg,Fe)_2SiO_4$) phase transitions are olivine $\rightarrow$ wadsleyite and wadsleyite $\rightarrow$ ringwoodite, respectively. At 660 km depth ringwoodite disproportionates into bridgmanite ($(Mg,Fe)SiO_3$) and ferropericlase

Table 1: **Properties and Minerals of the Earth***

depth (km)	pressure (GPa)	temperature (K)	phase transitions	mineralogy
100	3.32	1672	none	Ol, Opx, Cpx,Gt
410	13.4	1860	Ol $\rightarrow$ Wa	Wa, Maj
520	17.9	1942	Wa $\rightarrow$ Ri	Ri, Maj
670	23.9	1960	Ri $\rightarrow$ Br + FeP	Br, FeP, Dm
2650	127	2540	post-perovskite	post-perovskite
2891	136	4000	liquid metal alloy	FeNi + X% light element
5150	329	6000	solid metal alloy	FeNi + 0.5*X% light element

*See Figure 1 for further details. Ol = olivine, Opx = orthopyroxene, Cpx = clinopyroxene, Gt = garnet, Wa = wadsleyite, Maj = majorite, Ri = ringwoodite, Br = Bridgmanite, FeP = Ferropericlase, Dm = Davidmaoite. Mantle temperatures for the underside of the seismically defined boundaries are from (Katsura, 2022). Core temperatures are weakly defined ($\pm$500 K for OC and $\pm$1000 K for IC), with the inner core boundary (ICB) providing a limit based upon the solidification of iron at these pressures.

((Mg,Fe)O).

The seismically defined density of Earth's core is $\sim$10% less than that of an Fe,Ni alloy at comparable P–T conditions, indicating the presence of light element(s). An estimated of the amount of light element in the outer core (i.e., "X"%) is typically estimated to be between 8 and 10 wt%, or twice that in atomic %, but these numbers are not fixed. The proportion of light element depends on the outer core's temperature and its Δ density relative to pure Fe (solid Fe, as liquid iron measurements have not been accomplished at core P & T conditions).

The temperature profile for the Earth is best constrained by the mantle potential temperature at the surface ($\sim$1640 K) and at the phase change at 410 km ($\sim$1860 K) (Sarafian et al., 2017; Katsura, 2022). The temperature of the appearance of bridgmanite at 660 km depth (1960 K) is reasonably well constrained, however, some consider this depth to represent a compositional change in the mantle (e.g., Ballmer et al. (2017)). If so, then there should be a marked temperature discontinuity at this conductive boundary. In the model considered here, however, the upper and lower mantle have approximately the same major element composition and there is no temperature discontinuity. The lack of chemical and isotopic evidence for upper-lower mantle differentiation and seismic images of oceanic lithosphere penetrating the mantle transition zone and plunging deep into the mantle provide justification for this assumption.

Figure 2 presents a temperature profile for the Earth. The adiabatic temperature (T)

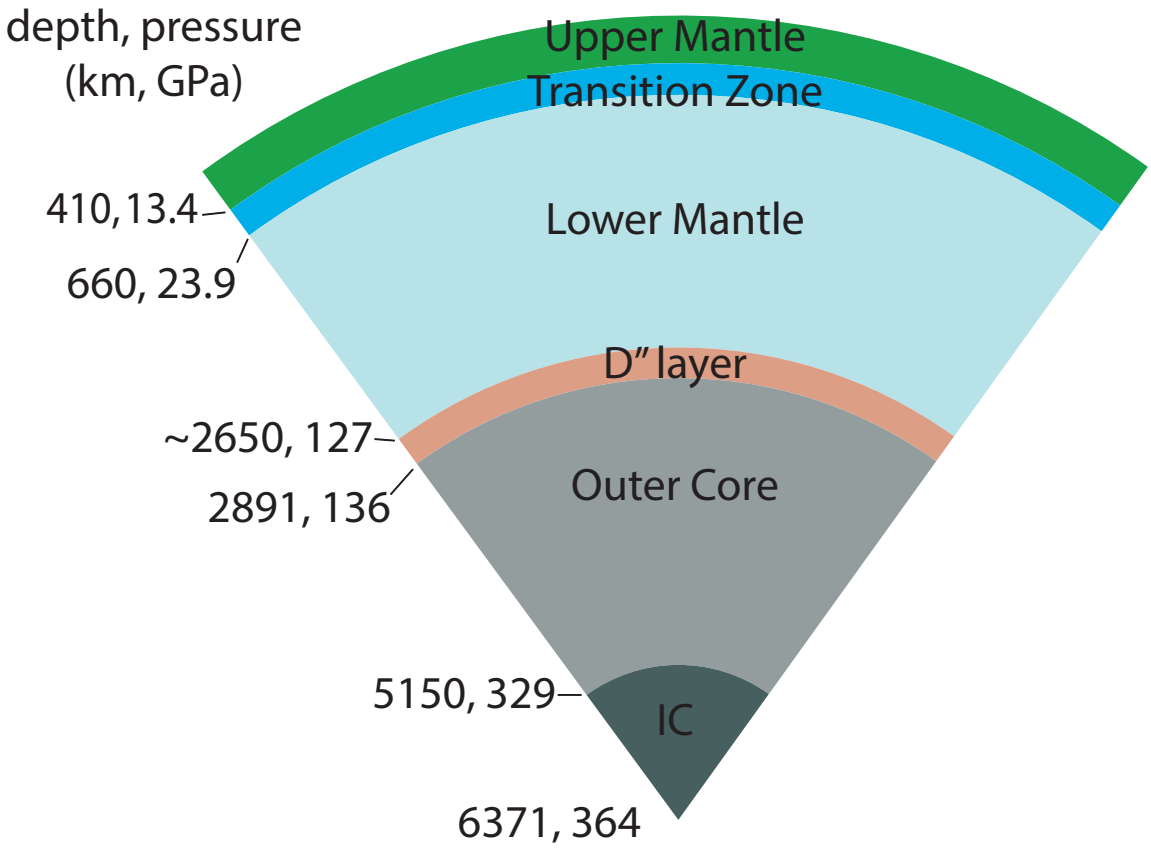

Fig. 1: The depth and pressure of phase changes in the mantle for an assumed pyrolite composition (McDonough and Sun, 1995). Similarly, conditions for the core are also presented. Depth and pressure values are taken from the PREM model (Dziewonski and Anderson, 1981). See Table 1 for further information.

gradient relative to depth (z) in the core and mantle is given as $(dT/dz) = \alpha g T/C_p$, where α is thermal expansivity (decreasing from 4×10^{-5} K^{-1} at the top of the mantle to 1×10^{-5} K^{-1} at D" (~2700 km depth)) (Katsura, 2022), g is gravitational acceleration (approximately constant for the mantle at ~9.8 m s^{-2}), and C_p is the isobaric heat capacity (~1000 J kg^{-1} s^{-1}). Values for α, T, and C_p in the metallic core are less well-known, with gravitational acceleration going to zero at the center of the Earth.

On average the adiabatic gradient for the mantle is ~0.3 K/km (from ~0.5 at the top of the mantle to ~0.25 at the bottom) and for the core is between 0.5 and 1.0 K/km. The core mantle boundary (CMB) represents a major temperature discontinuity and reflects conductive cooling across this interface. The core's temperature at the inner core boundary (ICB) and its adiabatic gradient sets the temperature at the core side of the CMB. Establishing the ICB temperature depends upon knowing the composition of the inner and outer core and crystallization temperature at 330 GPa. There continues to remain considerable uncertainty on the crystallization temperature of pure iron at ICB pressures (Williams et al., 1987; Tsuchiya et al., 2016; Kraus et al., 2022), which is the simplest analog composition for the inner core, albeit without a light element component.

1.3 The core, CMB, D", LLSVP, and ULVZ

The core and its boundary region represent an intriguing environment that is poorly understood. The core-mantle boundary (CMB) at 2891 km depth presents a sharp seismic discontinuity, defining the major attributes of the core (its size, density, state: liquid outer - solid inner core). Birch (1952) showed that the outer core's density is ~10% less than that of an Fe,Ni alloy at equivalent conditions, thus, documenting the core's density deficit. He concluded that the core must contain a proportion of one or more light elements, such as S, Si, O, C, and H. The outer core's density deficit depends on its temperature (Anderson and Isaak, 2002; Shanker et al., 2004), which is likely between 3500 and 6000 K, with 4000±500 K (McDonough, 2017) as the value often cited for the top of the outer core. The solid inner core represents only 4% by volume and 5% of the mass of the core, and it contains about half the amount of light element relative to the outer core (i.e., ~3–4% density deficit relative to pure Fe (Fei et al., 2016; Sakamaki et al., 2016)).

Earth's shape, mass, volume, bulk density, moment of inertia, and inner core libration are defined by geodetic studies, while geomagnetic studies show that outer core has maintained a geodynamo, of approximately its current state (variation in strength and polar stability), throughout most of its history. These observations constrain the structure and nature of the core. The presence of a PKJKP seismic wave and the absence of a shear wave demonstrates the outer core is liquid and the inner core is solid. A density increase (+820 kg/m^3) across the inner and outer core boundary is documented (Masters and Gubbins,

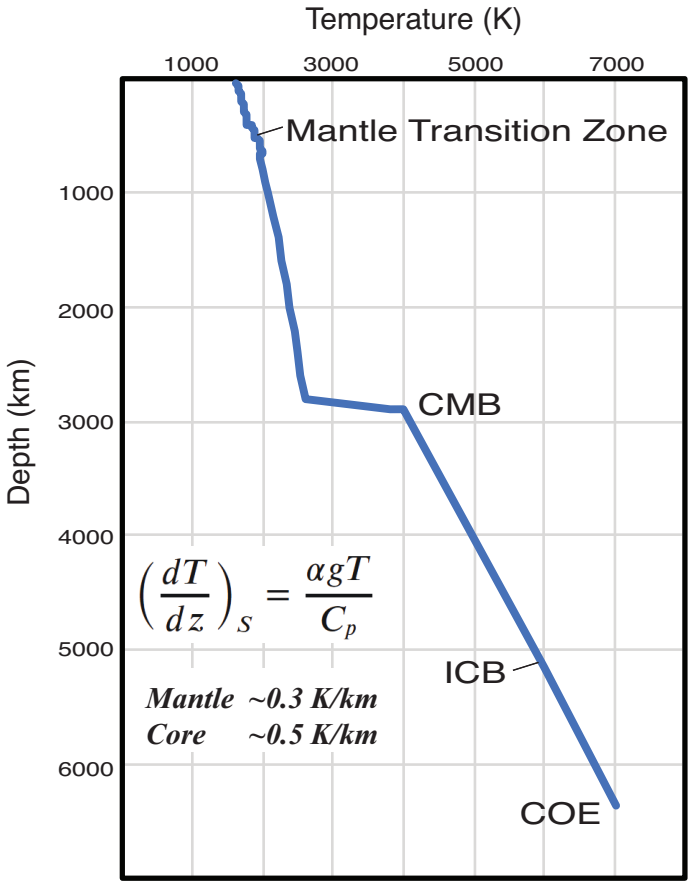

Fig. 2: The temperature profile for the Earth.

2003).

The D" region is a seismically defined (a reduction in Vp waves) region of the mantle that extends from the CMB upwards for ∼200 km and likely represents a conductive thermal boundary layer at the bottom of the mantle. Also sitting on the CMB are two other seismically identified entities: LLSVP (large low shear-wave velocity province, also called LLVP: large low velocity province) (Cottaar and Lekic, 2016; Kim et al., 2020) and ULVZ (ultra-low velocity zone) (Yu and Garnero, 2018). The two LLSVPs structures are antipodially positioned at near equatorial latitudes (beneath the central Pacific Ocean and south central Atlantic Ocean) and extend upward some 1500 km. Their sharp vertical seismic definitions are most consistent with these structures being chemical anomalies. It is also likely that this region is thermally distinct from the surrounding mantle. Many ocean islands, associated with hotspot upwellings, are believed to have source regions emanating from these LLSVPs (Jackson et al., 2021). Several ULVZ domains have been identified, which are much smaller pancake-like structures only a couple tens of kilometers across. Their distribution appears to be associated with the distal basal regions of the LLSVPs (Garnero et al., 2016).

1.4 The Mantle: 410 & 660 km deep seismic discontinuities

The Earth's mantle has two prominent, seismic discontinuities at 410 and 660 km depths, which define the Mantle Transition Zone (MTZ), and separates the upper and lower mantle. These seismic discontinuities are the product of mineralogical phase changes (see Section 1.2, Figure 1 and Table 1). The MTZ is considered to play a major role in the differentiation cycle in the mantle (Birch, 1952; Ringwood, 1994).

When entering the MTZ subducting oceanic lithosphere commonly bends and is laterally transported at or above the 660 km discontinuity. Some of these lithospheric domains later continue subducting into the lower mantle, while others may experience long-term residence in the MTZ. Importantly, the colder and markedly distinctive compositions of the basaltic and underlying harzburgitic layers of the subducting lithosphere means that it undergoes different depth dependent phase changes than that of the surrounding pyrolite-like mantle. Consequently, subducting lithosphere is distinctively more brittle and denser than the surrounding mantle, with the basaltic layer being denser than pyrolite in the MTZ and the harzburgite layer being denser than pyrolite just below the MTZ (Ringwood, 1994). These distinctive properties of subducted oceanic lithosphere play a significant role in mantle dynamics.

1.5 The lithosphere: crust and lithospheric mantle

The lithosphere is the thermal conductive layer at the top of the silicate Earth and is composed of crust and underlying lithospheric mantle. There are two different domains of lithospheres, oceanic and continental, and they have markedly different chemical, physical, and temporal attributes. The boundary between the crust and the mantle is reasonably well defined by the Moho seismic discontinuity, whereas the base of the lithosphere is poorly defined physically or chemically.

In the oceanic environment the average crust is basaltic, 50 million years old (with residual domains being up to 200 million years old), and typically 7 to 10 km thick. However, in some parts of the ocean the basaltic layer is absent (e.g., Central Atlantic and Southwest Indian Oceans) (Bonatti et al., 2001; Seyler et al., 2011). In contrast, the continental crust is on average andesitic in composition, 2+ billion years old (with residual domains being up to 4 billion years old), and typically ∼40 km thick (Rudnick and Gao, 2014; Sammon et al., 2022).

The thickness of the oceanic lithospheric mantle varies from zero at the mid ocean ridge spreading center to about 90 km thick beneath thermally mature oceanic crust. Compositionally, it varies from a highly depleted peridotite (i.e., dunite to harzburgite) at the top to a fertile lherzolite at its base. These compositional attributes reflect its generation via melt extraction at the ridges followed by off-ridge conductive cooling at its base. The thickness of the continental lithospheric mantle (CLM†) is also markedly variable depending upon its age and tectonic history. [†I pointedly avoid using the inaccurate term "subcontinental lithospheric mantle", as it implies the asthenosphere.] On average the continental lithospheric mantle appears to be ∼100 km thick beneath post-Archean terrains and ≥200 km thick beneath Archean terrains. Growth of the CLM is intimately linked with extraction of melt (crust formation) and the production of refractory peridotite. However, in contrast to the oceanic setting, the CLM was formed and evolved in multiple tectono-magmatic events.

2 Compositionally distinctive domains

2.1 The major elements (O, Fe, Mg, Si)

The Earth, the terrestrial planets, and chondrites have ∼93% of their masses and atomic proportions being composed of O, Fe, Mg and Si (Fig. 3) (Wasson and Kallemeyn, 1988; McDonough and Yoshizaki, 2021). The relative proportions of these 4 elements in ordinary, carbonaceous, enstatite, and G chondrites are not fixed. McDonough and Yoshizaki (2021) noted the variation in Mg/Si (∼25%), Fe/Si (factor of ≥2), and Fe/O (factor of ≥3)

between chondrite groups. Variability in these four elements is consistent with them being non-refractory elements (i.e., having 50% (half-mass) condensation temperatures $<$1350 K).

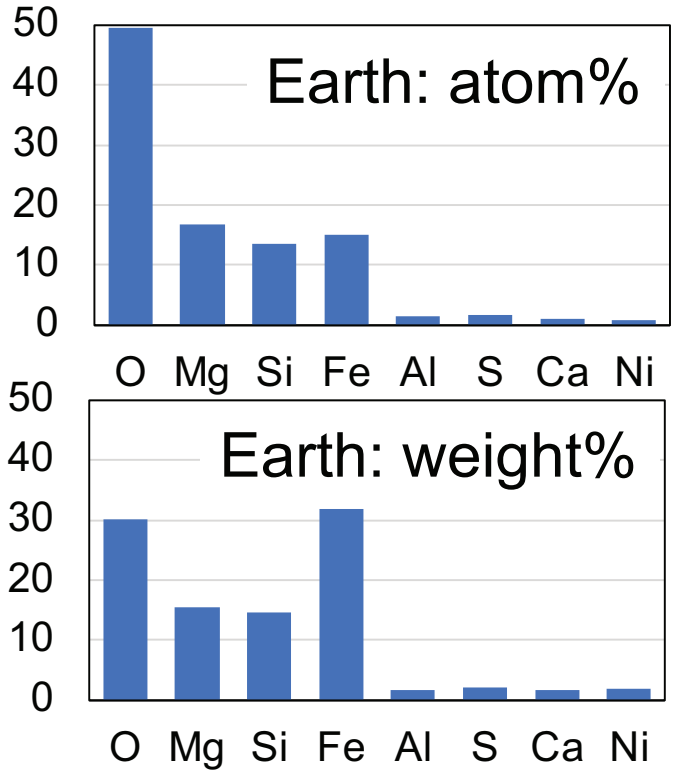

Fig. 3: The eight most abundant elements in the Earth.

2.2 The big 8 elements

In addition to the main group elements (i.e., O, Mg, Si, and Fe), there are four minor group elements (i.e., Al, Ca, S and Ni) that together constitute 99% the mass and atomic proportions of the Earth and terrestrial planets (Fig. 3). Both Al and Ca are refractory and present in chondritic proportions (Ca/Al = 1.07$\pm$0.04). Setting the abundance of either Al or Ca in the planet allows us to establish Earth's absolute abundances of all 37 refractory elements (McDonough and Sun, 1995). The value of Fe/Ni in chondrites is observed to be constant (17.4$\pm$0.5). Additional constrains come from the mass fraction of metallic core (32.5) and silicate Earth (67.5), the Mg# of the bulk silicate Earth (0.89), and the Ni content of the mantle. Thus, these rules allow us to put constraints on the bulk Earth composition.

To develop a model Earth composition requires additional constraints, specifically the sulfur content of, and the Fe/O and Mg/Si values for the bulk Earth and bulk silicate Earth. The core and mantle mass fraction constrains the Earth's Fe/O value, as the core contains >90% of Earth's iron and the mantle contains >90% of Earth's oxygen. The mantle is estimated to have only a few hundred ppm sulfur, whereas the core is estimated to have as much as 6 wt%. The remaining big unknown is the Mg/Si value for the bulk Earth and bulk silicate Earth.

Constraining the Mg/Si value for the bulk Earth and bulk silicate Earth has been a long-standing problem (Ringwood, 1989). There is no fixed Mg/Si ratio for chondrites, despite the often-quoted concept of assuming a chondritic Mg/Si. Values of this ratio for chondritic averages range from about 0.65 in EH (hi-iron enstatite chondrites) to about 0.95 in the Tagish Lake carbonaceous chondrite. This variation reflects the proportion of olivine (2:1 molar Mg/Si) to pyroxene (1:1 molar Mg/Si) and metallic Si in chondritic parent bodies. Active accretion disks in our galaxy show rapid grain growth in the inner disk region and radial variations in the relative proportions of olivine to pyroxene (van Boekel et al., 2004; Bouwman et al., 2010; D'Alessio et al., 2001).

Predicting a planet's bulk composition requires establishing the proportion of olivine to pyroxene in the bulk silicate shell. For the Earth this was best established on a plot of Mg/Si versus Al/Si, with mantle peridotites forming a linear, melt depletion trend (Jagoutz et al., 1979; Hart and Zindler, 1986). In this diagram the fertile end-member is at the intersection of the mantle (geochemical) and chondritic (cosmochemical) fractionation trends. These authors established the bulk silicate Earth's Mg/Si (1.1, metal weight ratio) and Al/Si (0.11) values.

The final step to establishing concentrations of these elements in the bulk silicate Earth and bulk Earth required determining the absolute concentrations of the refractory lithophile elements in the mantle. McDonough and Sun (1995), using melt depletion trends, determined that the bulk silicate Earth had 2.7 times CI carbonaceous chondrite abundances of the refractory lithophile elements.

Table 2 provides a preferred model composition of the eight most abundant element in the bulk Earth, core, and bulk silicate Earth (BSE). This model uses a pyrolite composition for the bulk silicate Earth and is comparable to the models developed in McDonough and Sun (1995) and Palme and O'Neill (2014). The core composition represents a revised estimate from McDonough (2017), now with a higher sulfur content and lower silicon and oxygen contents.

A simple compositional model for the Earth, assuming a CI chondrite composition, is presented in Table 3. This model is often justified by forcing a Mg/Si match to the solar photosphere's composition. This alternative model is not preferred as it requires a gross distinction between the upper and lower mantle compositions. Note all models accept that

Table 2: Composition of the Earth and its parts

	bulk Earth		core		BSE	
	wt%	at %	wt%	at %	wt%	at %
O	30.0	49.4	1.0	3.3	44.0	58.4
Mg	15.4	16.7	0	0	22.8	19.9
Si	14.5	13.6	1.0	1.9	21.0	15.9
Fe	31.9	15.0	85.3	79.7	6.3	2.4
Al	1.59	1.55	0	0	2.35	1.85
S	2.11	1.73	6.45	10.5	0.03	0.02
Ca	1.71	1.12	0	0	2.53	1.34
Ni	1.82	0.82	5.21	4.63	0.20	0.07
other	0.69	0.00	1.21	0.01	0.54	0.00
	99.8	100	100.1	100	99.9	100

Details given in McDonough (2014), which assumes a pyrolite model composition for the bulk silicate Earth (BSE). wt=weight, at=atoms. The at% columns were calculated from the wt% values and normalized to 100%. "other" includes Co, Cr and P for the bulk Earth and core, and Na, Cr and P for the bulk silicate Earth

the upper mantle has a pyrolite composition, which has been documented thoroughly. To maintain a pyrolite upper mantle there has to be limited mass exchange between the upper and lower mantles and a discontinuity in the mantle geothermal across this conductive boundary layer. These latter two observations appear to be at odds with seismic evidence (Fukao and Obayashi, 2013) and a mid-mantle viscosity discontinuity (Rudolph et al., 2015).

The core composition in this model was established based upon the sulfur content of CI, which adds a significant and unrealistic amount of light element (S) content to the core. It is also noteworthy that this model cannot accommodate any silicon or oxygen in the core.

This simple exercise shows the weaknesses associated with assuming a CI chondrite compositional model. Traditionally such models are justified based solely on the CI Mg/Si value matching that of the solar photosphere, which is taken to be representative of the mass of the solar system. However, an exact match of the bulk Earth to CI chondrite is impossible given the latter's volatile content (i.e., H_2O and CO_2). The usual convention is to create a degassed composition leaving behind some ad hoc amount of H and C in the BSE and core. Moreover, in this example one would have to also lose some amount sulfur to accommodate the totals and fit the core's $\sim$10% density deficit (Birch, 1952). Picking one element ratio to establish a planetary composition is fraught with many complications

and unwelcomed consequences.

Table 3: CI composition of the Earth and its parts

CI model	bulk Earth		core		BSE		upper mantle		lower mantle	
	wt%	at %	wt%	at %	wt%	at %	wt%	at %	wt%	at %
O	30.6	50.0	0	0	45.4	60.4	44.0	58.4	45.8	61.1
Mg	13.5	14.5	0	0	20.0	17.6	22.8	19.9	19.1	16.7
Si	15.3	14.2	0	0	22.7	17.2	21.0	15.9	23.3	17.7
Fe	26.4	12.3	75.5	62.5	5.9	2.3	6.3	2.4	5.8	2.2
Al	1.19	1.15	0	0	1.76	1.39	2.35	1.85	1.55	1.23
S	7.63	6.21	23.5	33.9	0.03	0.02	0.03	0.02	0.03	0.02
Ca	1.26	0.82	0	0	1.86	0.99	2.53	1.34	1.62	0.87
Ni	1.56	0.69	4.61	3.63	0.20	0.07	0.20	0.07	0.20	0.07
other	1.17	0.00	1.15	0.01	0.54	0.00	0.54	0.00	0.54	0.00
	98.7	100	104.7	100	98.5	100	99.9	100	97.9	100

Details for CI composition is given in Lodders (2020); this model represents a degassed composition with a final content of H and C being ∼2000 ppm in the BSE (bulk silicate Earth). The BSE was divided into a lower mantle and a combined upper mantle and transition zone (labeled upper mantle). A pyrolite model composition was assumed for this upper mantle (see Table 3). The at% columns were calculated from the wt% values and normalized to 100%. "other" includes Co, Cr and P for the bulk Earth and core, and Na, Cr and P for the bulk silicate Earth. wt=weight, at=atoms

It is also useful to consider the mineralogical composition of the lower mantle (Table 4). The lower mantle is primarily composed of three minerals: bridgmanite, ferropericlase, and davidmaoite. Davidmaoite is the calcium bearing perovskite ($CaSiO_3$), with a simple chemistry. Likewise, ferropericlase (Mg,Fe)O also has a simple chemistry and likely is a host for nickel in the mantle. The most abundant mineral in the Earth is bridgmanite ($(Mg,Fe^{2+},Fe^{3+},Al)SiO_{3.x}$), with the coefficient of 3.x to account for the charge balance needed for the substitution of Fe^{3+} and Al^{3+} for Mg^{2+} and Fe^{2+}

Presented in Table 4 are the mode proportions of bridgmanite, ferropericlase, and davidmaoite in a pyrolite model (Table 2) and a CI model (Table 3) composition for the lower mantle. The CI model assumes that the upper mantle and transition zone has a pyrolite composition. This compositional model for the mantle above 660 km is well documented in a wide range of mantle peridotite samples. The limited davidmaoite content of the lower mantle in this CI model means that this mantle composition has a lower mass fraction of refractory elements, including the heat producing elements U & Th.

Table 4: Lower mantle mineral proportions for 2 compositional models

	bridgmanite Mg-perovskite $(Mg,Fe^{2+},Fe^{3+},Al)SiO_{3.x}$	ferropericlase $(Mg,Fe)O$	davidmaoite Ca-pvk $CaSiO_3$
Pyrolite	74	19	7
CI-model	89	7	4

2.3 Heat producing elements (K, Th & U)

The Earth is a hybrid engine powered by two sources of energy: residual primordial energy, evolved from accretion and core separation, and heat from radioactive decay. Radiogenic heat production in the Earth overwhelming comes from ^{40}K, ^{232}Th, ^{238}U, and ^{235}U (i.e.,99.5% in total). The Earth's radiogenic power has been estimated at 20±3 TW, which assumes a specific model composition (McDonough and Sun, 1995; Palme and O'Neill, 2014). Predictions from competing compositional models span from 10 to 33 TW, thus, there are considerable uncertainties in our understanding of the absolute amount of radiogenic power in the Earth.

Both Th and U, like Ca and Al, are refractory lithophile elements, are assumed to be concentrated in the silicate Earth, and occur in chondritic proportions to one another. This means if we know the absolute concentration of one of these elements, then we know the absolute concentration of some 29 refractory lithophile elements.

McDonough and Sun (1995) found that cosmochemical (e.g., condensation and loss of volatiles) and geochemical (i.e., core formation) fractionation processes resulted in the bulk silicate Earth having an enrichment in refractory lithophile elements at 2.7 times that of an undegassed CI chondrite. Similarly, assuming instead a CI model for the composition of the bulk silicate Earth, this results in the refractory lithophile elements being enriched by 2.2 times relative to an undegassed CI chondrite. Consequently, these two different compositional models generate different amounts of radiogenic heat.

The amount of radiogenic heat in the Earth is now being determined at the global scale through the measurements the Earth's geoneutrino flux (Araki et al., 2005). Geoneutrino measurements are being conducted by particle physicists and provide a transformative-level discovery of the current composition and heat production in the Earth. These data provide insights into the thermal evolution of Earth and independently define the silicate Earth's enrichment factor from a CI chondrite composition.

Existing data from the two particle physics experiments predict that the Earth has either $14.6^{+5.2}_{-4.2}$ TW (KamLAND, Japan) (Abe et al., 2022) or $38.2^{+13.6}_{-12.7}$ TW (Borexino, Italy) (Agostini et al., 2020) total radiogenic power. More recently, however, the neutrino flux

measurement for Borexino has been re-interpreted with a more accurate with local lithospheric model. Sammon and McDonough (2022) showed that the initial geological model used by the Borexino physicists (Agostini et al., 2020) failed to recognize the abundant local igneous rocks that have high K, Th and U contents. By under-predicting the regional contribution of the geoneutrino flux the Borexino team over-predicted the global radiogenic budget of the Earth. Using a more accurate compositional model for the lithosphere surrounding Borexino results in a 20 TW Earth model (Sammon and McDonough, 2022).

The SNO+, Canada (Andringa et al., 2016) geoneutrino experiment is now counting and the JUNO, China (An et al., 2016) experiment is being built. Results from these experiments will provide additional data in the coming years and reduce the uncertainties for the mantle's radiogenic power. These data also define the composition of the silicate Earth and bulk Earth for the refractory elements.

3 Present day continental crust and modern mantle

The present day architecture of the silicate Earth has continental and oceanic crust surrounding a modern mantle composed of chemically and isotopically depleted and enriched domains. The oceanic crust is relatively simple, basaltic in composition, and a product of single stage melting of the mantle. In contrast, the continental crust is considerably more complicated. It is older, a product of multistage melting, and possesses an extraordinary range of rock compositions (e.g., sandstones to limestones and everything in between). On average the continental crust is andesitic ($\sim$60 wt%) in composition (Rudnick and Gao, 2014; Sammon et al., 2022). The depleted domain of the modern mantle is the MORB source region, which occupies a considerable mass fraction of the mantle ($\geq$70%), while the enriched domain, the remaining fraction, is the source region for Ocean Island Basalts (OIB).

The mass of the continental crust is 2.32 $\times 10^{22}$ kg and represents about 0.58% of the silicate Earth (Sammon et al., 2022). It covers around 44% of the surface area and is on average 41 km thick. The top of the crust is granitic in composition and from there, there is an SiO_2 gradient from $\sim$61 wt% (quartz monzonite) to $\sim$53 wt% (gabbronorite) from the middle to the base of the crust. Radiogenic heat production by the continental crust is estimated to be 330 picowatts/kg or 7.7 TW in total (Sammon et al., 2022), with the continental crust containing about 40% of the BSE budget of K, Th and U. The remaining 60% of these elements are in the modern mantle providing 12.3 TW to drive its geodynamic engine.

Our understanding of the modern mantle remains weak. We can identify two main magma types (MORB and OIB), which we interpreted as being derived from depleted and

enriched domains. The mass fraction, its distribution, and the composition of the depleted mantle is poorly constrained. It is possible that the depleted mantle is vertically stratified with more incompatible trace element depletions at the top of the mantle and more chemical fertility lower down. Such a chemical stratigraphy might explain differences between compositional models for the depleted mantle (Salters and Stracke, 2004; Workman and Hart, 2005) and the helium-heat flux paradox (O'Nions and Oxburgh, 1983).

The mass fraction, its distribution, and the composition of the enriched mantle is even less well understood than what we know about the depleted mantle. Current models for the enriched source regions of the OIB lavas envisage a significant role being played by the LLSVPs (Jackson et al., 2021), which are large degree-2, antipodial structures that are near-equatorial positions and extend up to 1500 km from core-mantle boundary. OIB lavas (e.g., some HIMU) and some continental intraplate basalts (e.g., recent basalts in eastern China) have been proposed as coming from recycled lithospheric components stored in the base of the transitions zone (Ringwood, 1982; Zhao et al., 2011; Huang et al., 2020).

4 Mantle geodynamics

Seismic tomography is providing a rich record of 2D and 3D images of the fate of subducting oceanic lithosphere as they penetrate deeper into the mantle. Some oceanic slabs stagnate at the base of the transition zone and are transported laterally for considerable distances. Fukao and Obayashi (2013) showed that others stagnate below 600 km and reside horizontally at $\sim$1000 km depth, while others plunge directly into the deep mantle. The reasons for these different dynamical responses are not clear, but may be related to density barriers (Ringwood, 1982) and viscosity filters (Rudolph et al., 2015) in this portion of the mantle.

These seismic images document considerable mass exchange between the upper and lower mantle and are consistent with whole mantle convection. The Mantle Transition Zone (MTZ) and several hundred km beneath it appears plays a major role in the differentiation of mantle. Understanding the dynamics of this region is essential (Ringwood, 1994).

Water is a significant unknown in the mantle, with compositional estimates ranging by an order of magnitude (Marty, 2012; Ohtani, 2021). Moreover, we are not certain if the net water flux is greater or lesser from mantle to surface over time. Mantle dynamics is controlled by it's viscosity, which in turn is controlled by its water content and temperature. The efforts of geoneutrino studies are focused on precisely defining the radiogenic heating curve for the history of the planet. This information will constrain the thermal evolution of the Earth and its viscosity structure.

There is considerable uncertainty on the initial thermal condition of the proto-Earth, especially regarding the timing of Moon formation, via collision with a Mars-sized bolide. Much depends on the presence or absence of an atmosphere, which has a blanketing effect on surface heat loss. In addition, the Earth's τ-accretion age is unknown. If the Earth's τ-accretion age is 10 million years, then as McDonough et al. (2020) showed ^{26}Al and ^{60}Fe played a significant role in heating of the planet and likely accelerated core formation. Subsequent to this early heating event was the Moon forming giant impact event, which is constrained to have occurred between 50 and 150 million years after t_{zero}, the age of calcium – aluminum inclusions which are the oldest formed solids in the solar system.

Developing a thermal model for the Earth can provide insights into early mantle differentiation products, including the existence of primordial reservoirs that may (or not) currently exist at the base of the mantle. The last 20 years of research into decay products of extinct short-lived nuclides (e.g., ^{142}Nd and ^{182}W) have provided many exciting new insights (Boyet and Carlson, 2005; Mundl et al., 2017), but these studies have also raised more questions than they have resolved.

Over the last several decades we have made great strides in measuring trace element abundances, radiogenic isotope compositions (e.g., Sr, Nd, Pb, Hf), and noble gas isotopic compositions (e.g., He, Ne, Ar, Xe) of modern basalts, including Mid Ocean Ridge Basalt (sampling the depleted mantle) and Ocean Island basalts (sampling the enriched mantle). Insights gained from these measurements coupled with detailed tomographic images from seismology (French and Romanowicz, 2015) have advanced our understanding of the architecture of the mantle (Jackson et al., 2017). More recently, we have added stable isotopes systems and extinct short-lived isotope systems to the repertoire of tools to investigate the mantle.

The ^{142}Nd isotope system ($^{146}\text{Sm} \rightarrow {}^{142}\text{Nd} + \alpha + \text{Q}$, $t_{1/2}$ = 103 Ma) and ^{182}W isotope system ($^{182}\text{Hf} \rightarrow {}^{182}\text{W} + 2e^- + 2\bar{\nu_e} + \text{Q}$, $t_{1/2}$ = 8.9 Ma) provide insights into early crust formation and core-mantle segregation, respectively. After about 6 half-lives, these isotope systems become extinct relative to our abilities of measurement. The ^{182}W isotope system records the fractionation of Hf (wholly stored in the mantle) from W (mostly ($\sim$90%) partitioned into the metallic core). It is predicted that the $(^{182}\text{W}/^{184}\text{W})_{core}$ is 200 ppm lighter than that of the surrounding mantle and that this isotopic difference was frozen into the core within the first 100 million years of Earth's history (Kleine and Walker, 2017).

Significantly, none of the Ocean Island Basalts recording Hadean evidence of ^{182}W/^{184}W isotopic anomalies contain any evidence of anomalous ^{142}Nd/^{144}Nd isotopic compositions (Mundl-Petermeier et al., 2020). Consequently, the source regions of basalts carrying Hadean isotopic signatures are likely much younger and are related to the recycling of oceanic crust subsequent to continent formation (Hofmann and White, 1982). In contrast, Eoarchean continental rocks are known to have ^{142}Nd/^{144}Nd isotopic anomalies. This has

led to the suggestion that these anomalous isotopic signatures are recently inheriting ^{182}W along with primitive helium from the core (Mundl et al., 2017; Mundl-Petermeier et al., 2020).

Evidence for the mechanism(s) of core-mantle exchange remains elusive. Documented Hadean ^{182}W/^{184}W isotopic anomalies coupled with primordial noble gas signatures in OIBs presents a preservation challenge for mantle convection models (Mundl et al., 2017). Understanding the formation, nature, long-term stability, and distribution of these components in the mantle remains a significant area of study.

References

Abe, S., Asami, S., Eizuka, M., Futagi, S., Gando, A., Gando, Y., Gima, T., Goto, A., Hachiya, T., Hata, K., Hosokawa, K., Ichimura, K., Ieki, S., Ikeda, H., Inoue, K., Ishidoshiro, K., Kamei, Y., Kawada, N., Kishimoto, Y., Koga, M., Kurasawa, M., Maemura, N., Mitsui, T., Miyake, H., Nakahata, T., Nakamura, K., Nakamura, K., Nakamura, R., Ozaki, H., Sakai, T., Sambonsugi, H., Shimizu, I., Shirahata, Y., Shirai, J., Shiraishi, K., Suzuki, A., Suzuki, Y., Takeuchi, A., Tamae, K., Watanabe, H., Yoshida, Y., Obara, S., Ichikawa, A.K., Yoshida, S., Umehara, S., Fushimi, K., Kotera, K., Urano, Y., Berger, B.E., Fujikawa, B.K., Learned, J.G., Maricic, J., Axani, S.N., Fu, Z., Smolsky, J., Winslow, L.A., Efremenko, Y., Karwowski, H.J., Markoff, D.M., Tornow, W., Li, A., Detwiler, J.A., Enomoto, S., Decowski, M.P., Grant, C., Song, H., O'Donnell, T., Dell'Oro, S., 2022. Abundances of uranium and thorium elements in earth estimated by geoneutrino spectroscopy. Geophysical Research Letters , e2022GL099566.

Agostini, M., Altenmüller, K., Appel, S., Atroshchenko, V., Bagdasarian, Z., Basilico, D., Bellini, G., Benziger, J., Biondi, R., Bravo, D., Caccianiga, B., Calaprice, F., Caminata, A., Cavalcante, P., Chepurnov, A., D'Angelo, D., Davini, S., Derbin, A., Di Giacinto, A., Di Marcello, V., Ding, X.F., Di Ludovico, A., Di Noto, L., Drachnev, I., Formozov, A., Franco, D., Galbiati, C., Ghiano, C., Giammarchi, M., Goretti, A., Göttel, A.S., Gromov, M., Guffanti, D., Ianni, A., Ianni, A., Jany, A., Jeschke, D., Kobychev, V., Korga, G., Kumaran, S., Laubenstein, M., Litvinovich, E., Lombardi, P., Lomskaya, I., Ludhova, L., Lukyanchenko, G., Lukyanchenko, L., Machulin, I., Martyn, J., Meroni, E., Meyer, M., Miramonti, L., Misiaszek, M., Muratova, V., Neumair, B., Nieslony, M., Nugmanov, R., Oberauer, L., Orekhov, V., Ortica, F., Pallavicini, M., Papp, L., Pelicci, L., Penek, Pietrofaccia, L., Pilipenko, N., Pocar, A., Raikov, G., Ranalli, M.T., Ranucci, G., Razeto, A., Re, A., Redchuk, M., Romani, A., Rossi, N., Schönert, S., Semenov, D., Settanta, G., Skorokhvatov, M., Singhal, A., Smirnov, O., Sotnikov, A., Suvorov, Y., Tartaglia, R., Testera, G., Thurn, J., Unzhakov, E., Villante, F.L., Vishneva, A., Vogelaar,

R.B., von Feilitzsch, F., Wojcik, M., Wurm, M., Zavatarelli, S., Zuber, K., Zuzel, G., 2020. Experimental evidence of neutrinos produced in the CNO fusion cycle in the Sun. Nature 587, 577–582. doi:10.1038/s41586-020-2934-0.

An, F., An, G., An, Q., Antonelli, V., Baussan, E., Beacom, J., Bezrukov, L., Blyth, S., Brugnera, R., Avanzini, M.B., Busto, J., Cabrera, A., Cai, H., Cai, X., Cammi, A., Cao, G., Cao, J., Chang, Y., Chen, S., Chen, S., Chen, Y., Chiesa, D., Clemenza, M., Clerbaux, B., Conrad, J., D'Angelo, D., Kerret, H.D., Deng, Z., Deng, Z., Ding, Y., Djurcic, Z., Dornic, D., Dracos, M., Drapier, O., Dusini, S., Dye, S., Enqvist, T., Fan, D., Fang, J., Favart, L., Ford, R., Göger-Neff, M., Gan, H., Garfagnini, A., Giammarchi, M., Gonchar, M., Gong, G., Gong, H., Gonin, M., Grassi, M., Grewing, C., Guan, M., Guarino, V., Guo, G., Guo, W., Guo, X.H., Hagner, C., Han, R., He, M., Heng, Y., Hsiung, Y., Hu, J., Hu, S., Hu, T., Huang, H., Huang, X., Huo, L., Ioannisian, A., Jeitler, M., Ji, X., Jiang, X., Jollet, C., Kang, L., Karagounis, M., Kazarian, N., Krumshteyn, Z., Kruth, A., Kuusiniemi, P., Lachenmaier, T., Leitner, R., Li, C., Li, J., Li, W., Li, W., Li, X., Li, X., Li, Y., Li, Y., Li, Z.B., Liang, H., Lin, G.L., Lin, T., Lin, Y.H., Ling, J., Lippi, I., Liu, D., Liu, H., Liu, H., Liu, J., Liu, J., Liu, J., Liu, Q., Liu, S., Liu, S., Lombardi, P., Long, Y., Lu, H., Lu, J., Lu, J., Lu, J., Lubsandorzhiev, B., Ludhova, L., Luo, S., Vladimir Lyashuk, Möllenberg, R., Ma, X., Mantovani, F., Mao, Y., Mari, S.M., McDonough, W.F., Meng, G., Meregaglia, A., Meroni, E., Mezzetto, M., Miramonti, L., Thomas Mueller, Naumov, D., Oberauer, L., Ochoa-Ricoux, J.P., Olshevskiy, A., Ortica, F., Paoloni, A., Peng, H., Jen-Chieh Peng, Previtali, E., Qi, M., Qian, S., Qian, X., Qian, Y., Qin, Z., Raffelt, G., Ranucci, G., Ricci, B., Robens, M., Romani, A., Ruan, X., Ruan, X., Salamanna, G., Shaevitz, M., Valery Sinev, Sirignano, C., Sisti, M., Smirnov, O., Soiron, M., Stahl, A., Stanco, L., Steinmann, J., Sun, X., Sun, Y., Taichenachev, D., Tang, J., Tkachev, I., Trzaska, W., van Waasen, S., Volpe, C., Vorobel, V., Votano, L., Wang, C.H., Wang, G., Wang, H., Wang, M., Wang, R., Wang, S., Wang, W., Wang, Y., Wang, Y., Wang, Y., Wang, Z., Wang, Z., Wang, Z., Wang, Z., Wei, W., Wen, L., Wiebusch, C., Wonsak, B., Wu, Q., Wulz, C.E., Wurm, M., Xi, Y., Xia, D., Xie, Y., Zhi-zhong Xing, Xu, J., Yan, B., Yang, C., Yang, C., Yang, G., Yang, L., Yang, Y., Yao, Y., Yegin, U., Yermia, F., You, Z., Yu, B., Yu, C., Yu, Z., Zavatarelli, S., Zhan, L., Zhang, C., Zhang, H.H., Zhang, J., Zhang, J., Zhang, Q., Zhang, Y.M., Zhang, Z., Zhao, Z., Zheng, Y., Zhong, W., Zhou, G., Zhou, J., Zhou, L., Zhou, R., Zhou, S., Zhou, W., Zhou, X., Zhou, Y., Zhou, Y., Zou, J., 2016. Neutrino physics with JUNO. Journal of Physics G: Nuclear and Particle Physics 43, 030401. doi:10.1088/0954-3899/43/3/030401.

Anderson, O., Isaak, D., 2002. Another look at the core density deficit of earth's outer core. Physics of the Earth and Planetary Interiors 131, 19–27.

Andringa, S., Arushanova, E., Asahi, S., Askins, M., Auty, D.J., Back, A.R., Barnard, Z., Barros, N., Beier, E.W., Bialek, A., Biller, S.D., Blucher, E., Bonventre, R., Braid, D., Caden, E., Callaghan, E., Caravaca, J., Carvalho, J., Cavalli, L., Chauhan, D., Chen, M., Chkvorets, O., Clark, K., Cleveland, B., Coulter, I.T., Cressy, D., Dai, X., Darrach, C., Davis-Purcell, B., Deen, R., Depatie, M.M., Descamps, F., Di Lodovico, F., Duhaime, N., Duncan, F., Dunger, J., Falk, E., Fatemighomi, N., Ford, R., Gorel, P., Grant, C., Grullon, S., Guillian, E., Hallin, A.L., Hallman, D., Hans, S., Hartnell, J., Harvey, P., Hedayatipour, M., Heintzelman, W.J., Helmer, R.L., Hreljac, B., Hu, J., Iida, T., Jackson, C.M., Jelley, N.A., Jillings, C., Jones, C., Jones, P.G., Kamdin, K., Kaptanoglu, T., Kaspar, J., Keener, P., Khaghani, P., Kippenbrock, L., Klein, J.R., Knapik, R., Kofron, J.N., Kormos, L.L., Korte, S., Kraus, C., Krauss, C.B., Labe, K., Lam, I., Lan, C., Land, B.J., Langrock, S., LaTorre, A., Lawson, I., Lefeuvre, G.M., Leming, E.J., Lidgard, J., Liu, X., Liu, Y., Lozza, V., Maguire, S., Maio, A., Majumdar, K., Manecki, S., Maneira, J., Marzec, E., Mastbaum, A., McCauley, N., McDonald, A.B., McMillan, J.E., Mekarski, P., Miller, C., Mohan, Y., Mony, E., Mottram, M.J., Novikov, V., O'Keeffe, H.M., O'Sullivan, E., Orebi Gann, G.D., Parnell, M.J., Peeters, S.J.M., Pershing, T., Petriw, Z., Prior, G., Prouty, J.C., Quirk, S., Reichold, A., Robertson, A., Rose, J., Rosero, R., Rost, P.M., Rumleskie, J., Schumaker, M.A., Schwendener, M.H., Scislowski, D., Secrest, J., Seddighin, M., Segui, L., Seibert, S., Shantz, T., Shokair, T.M., Sibley, L., Sinclair, J.R., Singh, K., Skensved, P., Sörensen, A., Sonley, T., Stainforth, R., Strait, M., Stringer, M.I., Svoboda, R., Tatar, J., Tian, L., Tolich, N., Tseng, J., Tseung, H.W.C., Van Berg, R., Vázquez-Jáuregui, E., Virtue, C., von Krosigk, B., Walker, J.M.G., Walker, M., Wasalski, O., Waterfield, J., White, R.F., Wilson, J.R., Winchester, T.J., Wright, A., Yeh, M., Zhao, T., Zuber, K., 2016. Current status and future prospects of the SNO+ experiment. Advances in High Energy Physics 2016, 6194250. doi:10.1155/2016/6194250.

Araki, T., Enomoto, S., Furuno, K., Gando, Y., Ichimura, K., Ikeda, H., Inoue, K., Kishimoto, Y., Koga, M., Koseki, Y., Maeda, T., Mitsui, T., Motoki, M., Nakajima, K., Ogawa, H., Ogawa, M., Owada, K., Ricol, J.S., Shimizu, I., Shirai, J., Suekane, F., Suzuki, A., Tada, K., Takeuchi, S., Tamae, K., Tsuda, Y., Watanabe, H., Busenitz, J., Classen, T., Djurcic, Z., Keefer, G., Leonard, D., Piepke, A., Yakushev, E., Berger, B.E., Chan, Y.D., Decowski, M.P., Dwyer, D.A., Freedman, S.J., Fujikawa, B.K., Goldman, J., Gray, F., Heeger, K.M., Hsu, L., Lesko, K.T., Luk, K.B., Murayama, H., O'Donnell, T., Poon, A.W.P., Steiner, H.M., Winslow, L.A., Mauger, C., McKeown, R.D., Vogel, P., Lane, C.E., Miletic, T., Guillian, G., Learned, J.G., Maricic, J., Matsuno, S., Pakvasa, S., Horton-Smith, G.A., Dazeley, S., Hatakeyama, S., Rojas, A., Svoboda, R., Dieterle, B.D., Detwiler, J., Gratta, G., Ishii, K., Tolich, N., Uchida, Y., Batygov, M., Bugg, W.,

Efremenko, Y., Kamyshkov, Y., Kozlov, A., Nakamura, Y., Karwowski, H.J., Markoff, D.M., Nakamura, K., Rohm, R.M., Tornow, W., Wendell, R., Chen, M.J., Wang, Y.F., Piquemal, F., 2005. Experimental investigation of geologically produced antineutrinos with kamland. Nature 436, 499–503. doi:10.1038/nature03980.

Ballmer, M.D., Houser, C., Hernlund, J.W., Wentzcovitch, R.M., Hirose, K., 2017. Persistence of strong silica-enriched domains in the Earth's lower mantle. Nature Geoscience 10, 236–240. doi:10.1038/ngeo2898.

Birch, F., 1952. Elasticity and constitution of the Earth's interior. Journal of Geophysical Research 57, 227–286. doi:10.1029/JZ057i002p00227.

van Boekel, R.J.H.M., Min, M., Leinert, C., Waters, L.B.F.M., Richichi, A., Chesneau, O., Dominik, C., Jaffe, W., Dutrey, A., Graser, U., , Henning, T., de Jong, J., Köhler, R., de Koter, A., Lopez, B., Malbet, F., Morel, S., Paresce, F., Perrin, G., Preibisch, T., Przygodda, F., Schöller, M., Wittkowski, M., 2004. The building blocks of planets within the 'terrestrial' region of protoplanetary disks. Nature 432, 479–482. doi:10.1038/nature03088.

Bonatti, E., Brunelli, D., Fabretti, P., Ligi, M., Portaro, R.A., Seyler, M., 2001. Steady-state creation of crust-free lithosphere at cold spots in mid-ocean ridges. Geology 29, 979–982.

Bouwman, J., Lawson, W.A., Juhász, A., Dominik, C., Feigelson, E.D., Henning, T., Tielens, A.G.G.M., Waters, L.B.F.M., 2010. The protoplanetary disk around the M4 star RECX 5: witnessing the influence of planet formation? The Astrophysical Journal Letters 723, L243–L247. doi:10.1088/2041-8205/723/2/L243.

Boyet, M., Carlson, R.W., 2005. ^{142}Nd evidence for early ($>$ 4.53 Ga) global differentiation of the silicate Earth. Science 309, 576–581. doi:10.1126/science.1113634.

Cottaar, S., Lekic, V., 2016. Morphology of seismically slow lower-mantle structures. Geophysical Supplements to the Monthly Notices of the Royal Astronomical Society 207, 1122–1136.

D'Alessio, P., Calvet, N., Hartmann, L., 2001. Accretion disks around young objects. III. Grain growth. The Astrophysical Journal 553, 321. doi:10.1086/320655.

Dziewonski, A.M., Anderson, D.L., 1981. Preliminary reference Earth model. Physics of the Earth and Planetary Interiors 25, 297–356. doi:10.1016/0031-9201(81)90046-7.

Fei, Y., Murphy, C., Shibazaki, Y., Shahar, A., Huang, H., 2016. Thermal equation of state of hcp-iron: Constraint on the density deficit of earth's solid inner core. Geophysical Research Letters 43, 6837–6843.

French, S.W., Romanowicz, B., 2015. Broad plumes rooted at the base of the earth's mantle beneath major hotspots. Nature 525, 95–99.

Fukao, Y., Obayashi, M., 2013. Subducted slabs stagnant above, penetrating through, and trapped below the 660 km discontinuity. Journal of Geophysical Research: Solid Earth 118, 5920–5938.

Garnero, E.J., McNamara, A.K., Shim, S.H., 2016. Continent-sized anomalous zones with low seismic velocity at the base of earth's mantle. Nature Geoscience 9, 481–489.

Hart, S.R., Zindler, A., 1986. In search of a bulk-Earth composition. Chemical Geology 57, 247–267. doi:10.1016/0009-2541(86)90053-7.

Hofmann, A.W., White, W.M., 1982. Mantle plumes from ancient oceanic crust. Earth and Planetary Science Letters 57, 421–436.

Huang, S., Tschauner, O., Yang, S., Humayun, M., Liu, W., Corder, S.N.G., Bechtel, H.A., Tischler, J., 2020. HIMU geochemical signature originating from the transition zone. Earth and Planetary Science Letters 542, 116323.

Jackson, M., Becker, T., Steinberger, B., 2021. Spatial characteristics of recycled and primordial reservoirs in the deep mantle. Geochemistry, Geophysics, Geosystems 22, e2020GC009525.

Jackson, M., Konter, J., Becker, T., 2017. Primordial helium entrained by the hottest mantle plumes. Nature 542, 340–343.

Jagoutz, E., Palme, H., Baddenhausen, H., Blum, K., Cendales, M., Dreibus, G., Spettel, B., Lorenz, V., Wänke, H., 1979. The abundances of major, minor and trace elements in the earth's mantle as derived from primitive ultramafic nodules, in: Lunar and Planetary Science Conference Proceedings, pp. 2031–2050.

Katsura, T., 2022. A revised adiabatic temperature profile for the mantle. Journal of Geophysical Research: Solid Earth 127, e2021JB023562.

Kim, D., Lekić, V., Ménard, B., Baron, D., Taghizadeh-Popp, M., 2020. Sequencing seismograms: A panoptic view of scattering in the core-mantle boundary region. Science 368, 1223–1228.

Kleine, T., Walker, R.J., 2017. Tungsten isotopes in planets. Annual review of earth and planetary sciences 45, 389–417.

Kraus, R.G., Hemley, R.J., Ali, S.J., Belof, J.L., Benedict, L.X., Bernier, J., Braun, D., Cohen, R., Collins, G.W., Coppari, F., et al., 2022. Measuring the melting curve of iron at super-earth core conditions. Science 375, 202–205.

Lodders, K., 2020. Solar Elemental Abundances, in: Read, P. (Ed.), Oxford Research Encyclopedia of Planetary Science. Oxford University Press, Oxford, pp. 1–68. doi:10.1093/acrefore/9780190647926.013.145.

Marty, B., 2012. The origins and concentrations of water, carbon, nitrogen and noble gases on Earth. Earth and Planetary Science Letters 313, 56–66. doi:10.1016/j.epsl.2011.10.040.

Masters, G., Gubbins, D., 2003. On the resolution of density within the Earth. Physics of the Earth and Planetary Interiors 140, 159–167. doi:10.1016/j.pepi.2003.07.008.

McDonough, W.F., 2014. Compositional model for the Earth's core, in: Carlson, R.W. (Ed.), The Mantle and Core. Elsevier, Oxford. Treatise on Geochemistry (Second Edition). chapter 16, pp. 559–577. doi:10.1016/B978-0-08-095975-7.00215-1. editors-in-chief H. D. Holland and K. K. Turekian.

McDonough, W.F., 2017. Earth's core, in: White, W.M. (Ed.), Encyclopedia of Geochemistry: A Comprehensive Reference Source on the Chemistry of the Earth. Springer International Publishing, Cham, pp. 1–13. doi:10.1007/978-3-319-39193-9_258-1.

McDonough, W.F., Sun, S.S., 1995. The composition of the Earth. Chemical Geology 120, 223–253. doi:10.1016/0009-2541(94)00140-4.

McDonough, W.F., Šrámek, O., Wipperfurth, S.A., 2020. Radiogenic power and geoneutrino luminosity of the Earth and other terrestrial bodies through time. Geochemistry, Geophysics, Geosystems 21, e2019GC008865. doi:10.1029/2019GC008865.

McDonough, W.F., Yoshizaki, T., 2021. Terrestrial planet compositions controlled by accretion disk magnetic field. Progress in Earth and Planetary Science 8, 39. doi:10.1186/s40645-021-00429-4.

Mundl, A., Touboul, M., Jackson, M.G., Day, J.M., Kurz, M.D., Lekic, V., Helz, R.T., Walker, R.J., 2017. Tungsten-182 heterogeneity in modern ocean island basalts. Science 356, 66–69.

Mundl-Petermeier, A., Walker, R., Fischer, R., Lekic, V., Jackson, M., Kurz, M., 2020. Anomalous 182w in high 3he/4he ocean island basalts: Fingerprints of earth's core? Geochimica et Cosmochimica Acta 271, 194–211.

Ohtani, E., 2021. Hydration and dehydration in earth's interior. Annual Review of Earth and Planetary Sciences 49, 253–278.

O'Nions, R., Oxburgh, E., 1983. Heat and helium in the Earth. Nature 306, 429–431.

Palme, H., O'Neill, H.S.C., 2014. Cosmochemical estimates of mantle composition, in: Carlson, R.W. (Ed.), The Mantle and Core. Elsevier, Oxford. volume 3 of *Treatise on Geochemistry (Second Edition)* of *Treatise on Geochemistry (Second Edition)*. chapter 1, pp. 1–39. doi:10.1016/B978-0-08-095975-7.00201-1. editors-in-chief H. D. Holland and K. K. Turekian.

Ringwood, A., 1989. Significance of the terrestrial Mg/Si ratio. Earth and Planetary Science Letters 95, 1–7.

Ringwood, A., 1994. Role of the transition zone and 660 km discontinuity in mantle dynamics. Physics of the Earth and Planetary Interiors 86, 5–24.

Ringwood, A.E., 1982. Phase transformations and differentiation in subducted lithosphere: Implications for mantle dynamics, basalt petrogenesis, and crustal evolution. The Journal of Geology 90, 611–643.

Rudnick, R.L., Gao, S., 2014. Composition of the continental crust, in: Holland, H.D., Turekian, K.K. (Eds.), Treatise on Geochemistry (Second Edition). Elsevier, Oxford, pp. 1–51. doi:10.1016/B978-0-08-095975-7.00301-6.

Rudolph, M.L., Lekić, V., Lithgow-Bertelloni, C., 2015. Viscosity jump in Earth's mid-mantle. Science 350, 1349–1352.

Sakamaki, T., Ohtani, E., Fukui, H., Kamada, S., Takahashi, S., Sakairi, T., Takahata, A., Sakai, T., Tsutsui, S., Ishikawa, D., et al., 2016. Constraints on earth's inner core composition inferred from measurements of the sound velocity of hcp-iron in extreme conditions. Science Advances 2, e1500802.

Salters, V.J., Stracke, A., 2004. Composition of the depleted mantle. Geochemistry, Geophysics, Geosystems 5.

Sammon, L.G., McDonough, W.F., 2022. Quantifying earth's radiogenic heat budget. Earth and Planetary Science Letters 593, 117684.

Sammon, L.G., McDonough, W.F., Mooney, W.D., 2022. Compositional attributes of the deep continental crust inferred from geochemical and geophysical data. Journal of Geophysical Research: Solid Earth 127, e2022JB024041.

Sarafian, E., Gaetani, G.A., Hauri, E.H., Sarafian, A.R., 2017. Experimental constraints on the damp peridotite solidus and oceanic mantle potential temperature. Science 355, 942–945. doi:10.1126/science.aaj2165.

Seyler, M., Brunelli, D., Toplis, M.J., Mével, C., 2011. Multiscale chemical heterogeneities beneath the eastern southwest indian ridge (52 e–68 e): Trace element compositions of along-axis dredged peridotites. Geochemistry, Geophysics, Geosystems 12.

Shanker, J., Singh, B., Srivastava, S., 2004. Volume–temperature relationship for iron at 330 GPa and the Earth's core density deficit. Physics of the Earth and Planetary Interiors 147, 333–341.

Tsuchiya, T., Kawai, K., Wang, X., Ichikawa, H., Dekura, H., 2016. Temperature of the lower mantle and core based on ab initio mineral physics data. Deep Earth: Physics and Chemistry of the Lower Mantle and Core , 13–30.

Wasson, J.T., Kallemeyn, G.W., 1988. Compositions of chondrites. Philosophical Transactions of the Royal Society of London A: Mathematical, Physical and Engineering Sciences 325, 535–544. doi:10.1098/rsta.1988.0066.

Williams, Q., Jeanloz, R., Bass, J., Svendsen, B., Ahrens, T.J., 1987. The melting curve of iron to 250 gigapascals: A constraint on the temperature at earth's center. Science 236, 181–182.

Workman, R.K., Hart, S.R., 2005. Major and trace element composition of the depleted MORB mantle (DMM). Earth and Planetary Science Letters 231, 53–72.

Yu, S., Garnero, E.J., 2018. Ultralow velocity zone locations: A global assessment. Geochemistry, Geophysics, Geosystems 19, 396–414.

Zhao, D., Yu, S., Ohtani, E., 2011. East asia: Seismotectonics, magmatism and mantle dynamics. Journal of Asian Earth Sciences 40, 689–709.